remote sensing

MDPI

Article

Electromagnetic Field of a HED in the Spherical "Earth-Ionosphere" Model and Its Application in Geophysics

Ya Gao [1], Qing-Yun Di [1,2,3,*], Chang-Min Fu [1,2,3] and Yi-Lang Zhang [1,2,3]

[1] CAS Engineering Laboratory for Deep Resources Equipment and Technology, Institute of Geology and Geophysics, Chinese Academy of Sciences, Beijing 100029, China; gaoya@mail.iggcas.ac.cn (Y.G.)
[2] Innovation Academy for Earth Science, Chinese Academy of Sciences, Beijing 100029, China
[3] College of Earth and Planetary Sciences, University of Chinese Academy of Sciences, Beijing 100049, China
* Correspondence: qydi@mail.iggcas.ac.cn

Abstract: The controlled source extremely low frequency (CSELF) method bears the potential for deep resource exploitation utilizing the skywave. The "Skywave" denotes the electromagnetic wave propagating through the waveguide formed by the Earth and ionosphere. It has a considerable penetration depth into the lithosphere due to its low-frequency band. Previous research on extremely low-frequency electromagnetic fields with the coupled lithosphere, atmosphere, and planar ionosphere models ignored the effect of the Earth's curvature. Thus, we aimed to present the exact formulas for horizontal electric dipoles (HED) in a spherical "Earth-ionosphere" model. These new formulas consider the Earth's curvature as a multilayer medium rather than a homogeneous underground. We introduce three techniques: function combination pairs, addition and subtraction terms, and Padé approximants, to handle slow convergence in numerical calculation. In the spherical waveguide, electromagnetic fields are mutually interfered with and produce oscillations, which is different from the planar model. The influence of Earth's curvature cannot be neglected with the increase in source–receiver distance, though it is negligible within 3000 km. Furthermore, it is worth noting that apparent resistivity $\rho_{\theta\varphi}$ enters the waveguide area earlier than $\rho_{\varphi\theta}$. This method can be used as Green's function to simulate the electromagnetic field of actual antennas and 3-D models.

Keywords: controlled source extremely low frequency; deep mineral resources; spherical Earth-ionosphere model; electromagnetic field

check for updates

Citation: Gao, Y.; Di, Q.-Y.; Fu, C.-M.; Zhang, Y.-L. Electromagnetic Field of a HED in the Spherical "Earth-Ionosphere" Model and Its Application in Geophysics. *Remote Sens.* **2023**, *15*, 2235. https://doi.org/10.3390/rs15092235

Academic Editor: Angelo De Santis

Received: 13 March 2023
Revised: 18 April 2023
Accepted: 21 April 2023
Published: 23 April 2023

Copyright: © 2023 by the authors. Licensee MDPI, Basel, Switzerland. This article is an open access article distributed under the terms and conditions of the Creative Commons Attribution (CC BY) license (https://creativecommons.org/licenses/by/4.0/).

1. Introduction

Controlled source is an extremely low-frequency electromagnetic field emitted by a 100-km-long horizontal dipole source with a power output of up to megawatts and a transmission frequency range of 0.1–300 Hz. Electromagnetic waves propagate forward through the spherical air waveguide due to the large electrical resistivity contrast between the Earth and air and between the ionosphere and air, also known as the "skywave", shown in Figure 1a. The "Skywave" was first used by researchers in the United States and the Soviet Union for submarine communications and other military purposes. Therefore, they began to study the propagation of skywaves on Earth [1–5]. Communication between the ocean and land is challenging due to the high-frequency electromagnetic signals' rapid attenuation in seawater [6]. This issue is resolved using low-frequency (3–30 kHz) electromagnetic (VLF-EM) waves emitted by high-voltage wire [7–9]. The frequency band in VLF-EM wave propagation theory is naturally extended to super low-frequency (SLF) (300–30 Hz) and extremely low-frequency (ELF) (30–3 Hz) EM propagation to increase the depth of underwater communication [10–16]. Since the 1970s, many studies have been on wave propagation in a spherical earth. Here, the Earth is treated as a sphere rather than a planar ground [17–20]. In those studies, the internal structures of the Earth are ignored; rather, the Earth is considered a uniform sphere [21–26]. Though the simplified

earth model lays a fundamental foundation for understanding the CSELF fields, the model does not have much use for geophysical exploration because of the lack of the Earth's internal structure.

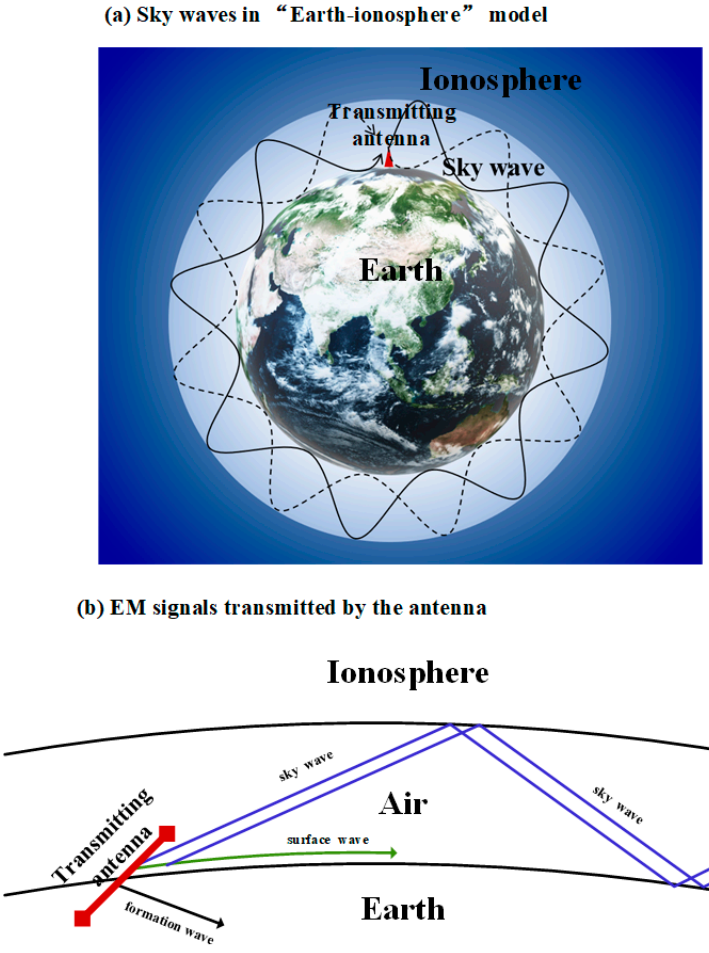

Figure 1. Electromagnetic field in the spherical "Earth-ionosphere" full space model (**a**) Sky waves in the "Earth-ionosphere" model: Solid and dashed lines represent sky waves propagating through different paths in a waveguide. (**b**) EM signals transmitted by the antenna: artificial sources generate three types of electromagnetic waves throughout full space: the sky wave, surface wave, and formation wave.

The skywave has a high potential for resource exploration because of its deep penetration into the lithosphere. In order to utilize the skywave to detect underground structures, geophysicists have proposed a new controlled source electromagnetic method: Controlled source extremely low frequency (CSELF) [27–32]. CSELF combines the advantages of magnetotellurics (MT) and controlled source audio-frequency magnetotellurics (CSAMT), which have a considerable detection depth and a high signal-to-noise ratio [31]. Accurate theories and calculation techniques must be developed to interpret the field data. Several pioneers on CSELF established an "Earth-ionosphere" horizontal model that consists of the ionosphere and the Earth's multilayer to simplify the mathematical complexity of the electromagnetic field in a spherical waveguide [30,31,33]. However, the model does not consider the curvature of the Earth. To overcome these limitations, we consider the Earth's curvature and include a spherically layered medium in the Earth. The new model establishes a framework for the geophysical purposes of the CSELF method.

The primary goal of this study is to establish an analytical solution for wave propagation by a horizontal electric dipole (HED) source on the surface of the spherical Earth used in the CSELF method. The new solution differs from that of Srivastava [34] and Gao [35]

for a vertical electric dipole; the latter does not have much use in the CSELF method. In addition, this method is not limited to calculating the electromagnetic field on the Earth's surface [36]; it can also calculate the electromagnetic field inside the Earth, which is very useful for three-dimensional modelling. Taking into account the fact that the actual ionosphere is not a uniform medium, the model utilized in the formula derivation contained ionospheric vertical non-uniformity, as shown in Figure 2b, which can be used to study the layered structure of the ionosphere. In this work, we introduce three techniques: function combination pair, "addition and subtraction term," and Padé approximant [35,37], to ease the cost and further achieve a performance boost of 1000 times. Based on these results, which are notably different from the planar model, we have studied its physical mechanism and provided theoretical guidance for field data acquisition. We further investigated the influence of the ionospheric structure on electromagnetic fields. At the end of this work, we discussed the application of Cagniard's apparent resistivity to the CSELF.

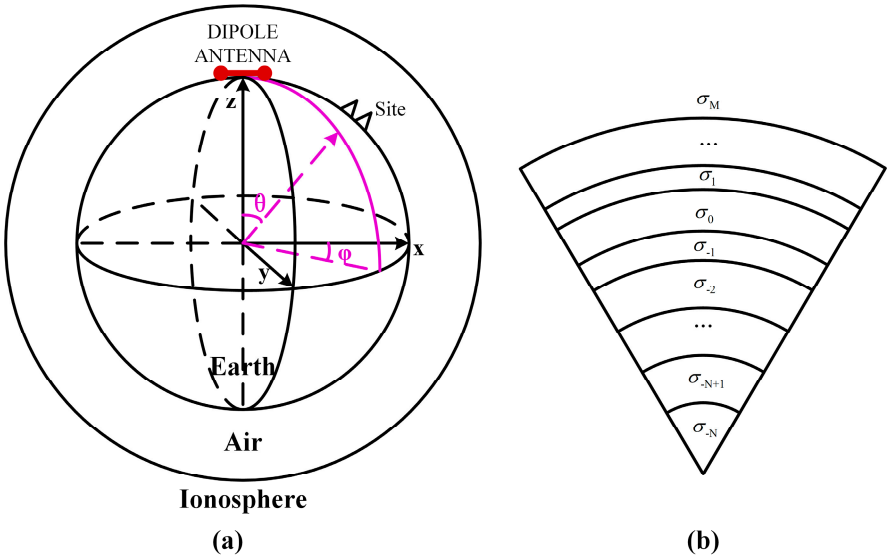

Figure 2. Geometric model diagram of HED in spherical coordinates. (**a**) Simplified spherical "Earth-ionosphere" full space model; (**b**) Multilayer medium inside the Earth or ionosphere: the subscript 0 indicates the medium where the source is located.

2. Materials and Methods

As shown in Figure 1b, the horizontal antenna will generate formation waves that propagate underground, surface waves that propagate along the Earth's surface, and sky waves that propagate upward in the air until they are reflected back to the ground through the ionosphere. In CSELF, sky waves are used to study the underground electrical structure. Thus, the source–receiver distance reaches thousands of kilometers [38].

2.1. Spherical "Earth-Ionosphere" Full-Space Model

In order to deduce the formulas of the electromagnetic field emitted by the CSELF source in the spherical "Earth-ionosphere" model, we simplified the artificial source to a horizontal electric dipole (HED), as shown in Figure 2. Considering the vertical anisotropic nature of the Earth and ionosphere, our model consists of multilayer media, and all layers in the model are isotropic media as well.

To make the formula, including four curl operators in spherical coordinates [35], more concise, we introduce a coordinate system with the spherical center as the origin, while the axis of the HED (of dipole moment dl) is oriented in the x direction, and it is assumed to carry a constant current I. In this coordinate, we used the relationship between the magnetic vector potential **A** and the electric dipole source (Equations (3)–(5)) to derive the expression of the primary field without curls.

The HED is located at $(r', 0, 0)$, and the receiver is located at (r, θ, φ). The axes of the cartesian coordinate pass through $(r', \pi/2, 0)$ $(r', \pi/2, \pi/2)$, $(r', 0, 0)$. We denote the medium where the HED is located as the ^{0t}h medium. The distance from the top interface of each layer to the center is a_i.

2.2. Derivation of the Formulas

With the time-harmonic factor $e^{-i\omega t}$, $i = \sqrt{-1}$, and the Debye potential π_e and π_m, the electromagnetic wave is divided into TM and TE waves [39], and the fields are expressed as follows:

$$\begin{array}{l} \mathbf{E} = \frac{1}{\sigma - i\omega\varepsilon}\nabla \times \nabla \times \mathbf{r}\pi_e - \nabla \times \mathbf{r}\pi_{\mathrm{m}} \\ \mathbf{H} = \nabla \times \mathbf{r}\pi_e - \frac{1}{i\omega\mu}\nabla \times \nabla \times \mathbf{r}\pi_{\mathrm{m}} \end{array} \tag{1}$$

where σ is the conductivity of the medium, ω is the angular frequency, ε is the dielectric constant, μ is the permeability of the medium, **E** is the electric vector, and **H** is the magnetic vector.

The Green's function of the uniform space is expressed as follows, to ensure that the time t of the field lags the time of the source:

$$G(r, r') = \frac{e^{ikR}}{4\pi R} \tag{2}$$

According to the relationship between the magnetic vector potential **A** and the electric dipole source:

$$\mathbf{A} = A_x \mathbf{e}_{\mathbf{x}} = \frac{Idl}{4\pi}\frac{e^{ikR}}{R}e_x \tag{3}$$

$$ikh_0^{(1)}(kr) = \frac{e^{ikr}}{r} \tag{4}$$

Therefore,

$$\begin{array}{l} \mathbf{A} = A_x \mathbf{e}_{\mathbf{x}} = \frac{Idl}{4\pi} ikh_0^{(1)}(k|r - r'|)\mathbf{e}_{\mathbf{x}} \\ h_0^{(1)}(k|r - r'|) = \sum\limits_{n=0}^{\infty}(2n+1)j_n(kr<)h_n^{(1)}(kr>)P_n(\cos\xi) \\ \cos\xi = \cos\theta\cos\theta' + \sin\theta\sin\theta'\cos(\varphi - \varphi') \end{array} \tag{5}$$

where R is the distance between the receiver and the source, k is the wave number, $k^2 = i\omega\mu(\sigma - i\omega\varepsilon)$, $h_0^{(1)}$ is the 0 order spherical Hankel function, dl is the electric dipole moment, $r>$ and $r<$ are the larger and smaller of the radial coordinate of the source and the receiver, respectively, and $P_n(x)$ is the Legendre function.

The primary field is obtained by transforming the magnetic vector into spherical coordinates:

$$\begin{array}{l} r\pi_m = -\frac{Idl\omega\mu}{4\pi k r'}\sin\varphi \\ \quad \sum\limits_{n=1}^{\infty}\frac{(2n+1)}{n(n+1)}J_n(kr<)H_n^{(1)}(kr>)P_n^1(\cos\theta) \\ r\pi_e = \frac{Idl(\sigma - i\omega\varepsilon)}{4\pi\omega\varepsilon k r'}\cos\varphi \\ \quad \sum\limits_{n=1}^{\infty}\frac{(2n+1)}{n(n+1)}\frac{\partial}{\partial r'}J_n(kr<)H_n^{(1)}(kr>)P_n^1(\cos\theta) \\ J_n(x) = xj_n(x) \\ H_n^{(1)}(x) = xh_n^{(1)}(x) \end{array} \tag{6}$$

where $j_n(x)$ is the n-order spherical Bessel function, and $h_n^{(1)}(x)$ is the n-order spherical Hankel function.

The Debye potential π_e and π_m satisfy the Helmholtz equation. In the spherical coordinate, the basic form of the general solution is obtained by separating variables:

$$\begin{bmatrix} \pi_e \\ \pi_m \end{bmatrix} = [\mathbf{a}J_n(\mathrm{kr}) + \mathbf{b}H_n^{(1)}(\mathrm{kr})]\mathrm{P}_n^m(\cos\theta)e^{im\varphi} \tag{7}$$

where **a** and **b** are two-dimensional column vectors, and $\mathrm{P}_n^m(\cos\theta)$ is the associated Legendre function.

The reflection and transmission of the primary field of the source generate the electromagnetic field in the passive region. The orthogonality of $\mathrm{P}_n^m(\cos\theta)$ and $e^{im\varphi}$ means that all waves are decoupled. Thus, the general solution of the passive region should be the same as the form of the primary field:

$$\begin{aligned} r\pi_e &= \tfrac{Idl(\sigma_0 - i\omega\varepsilon_0)}{4\pi\omega\varepsilon_0 k_0 r'}[a_n J_n(kr) + b_n H_n^{(1)}(kr)]\mathrm{P}_n^1(\cos\theta)\cos\varphi \\ r\pi_m &= -\tfrac{Idl\omega\mu}{4\pi k_0 r'}[c_n J_n(kr) + d_n H_n^{(1)}(kr)]\mathrm{P}_n^1(\cos\theta)\sin\varphi \end{aligned} \tag{8}$$

The boundary condition adopted is a general boundary condition where the tangential electromagnetic field is continuous, and the mathematical expression follows:

$$\begin{aligned} &r\pi_{e1} = r\pi_{e2} \\ &\tfrac{1}{\sigma_1 - i\omega\varepsilon_1}\tfrac{\partial}{\partial r}r\pi_{e1} = \tfrac{1}{\sigma_2 - i\omega\varepsilon_2}\tfrac{\partial}{\partial r}r\pi_{e2} \\ &r\pi_{m1} = r\pi_{m2} \\ &\tfrac{1}{\mu_1}\tfrac{\partial}{\partial r}r\pi_{m1} = \tfrac{1}{\mu_2}\tfrac{\partial}{\partial r}r\pi_{m2} \end{aligned} \tag{9}$$

The definite solution is the general solution plus the special solution. Given the boundary conditions, we derive the formulas of the electromagnetic field at an arbitrary point in the spherical "Earth-ionosphere" model.

$$\begin{aligned} r\pi_{mi} &= -\tfrac{Idl\omega\mu_0}{4\pi k_0 b}\sin\varphi\sum_{n=1}^{\infty}\tfrac{(2n+1)}{n(n+1)}F_m(r)T_{0,i}^{TE}M_i^{TE}M_0^{TE}P_n^1(\cos\theta) \\ F_m(r) &= [J_n(k_i r) + \widetilde{R}_{i,i-1}^{TE}H_n^{(1)}(k_i r)][H_n^{(1)}(k_0 b) + R_{0,-1}^{TE}J_n(k_0 b)] \\ r\pi_{ei} &= \tfrac{Idl(\sigma_0 - i\omega\varepsilon_0)}{4\pi\omega\varepsilon_0 k_0 b}\cos\varphi\sum_{n=1}^{\infty}\tfrac{(2n+1)}{n(n+1)}F_e(r)T_{0,i}^{TM}M_i^{TM}M_0^{TM}P_n^1(\cos\theta) \\ F_e(r) &= [J_n(k_i r) + \widetilde{R}_{i,i-1}^{TM}H_n^{(1)}(k_i r)][H_n'(k_0 b) + R_{0,-1}^{TM}J_n'(k_0 b)] \end{aligned} \tag{10}$$

where $\widetilde{R}$ is the generalized reflection coefficient, T is the generalized transmission coefficient and the influence factor of each layer due to multiple reflections in multilayered media [35]. See Appendix A for a detailed expression of the coefficient.

2.3. Numerical Calculation

The formulas include a spherical Bessel function and an associated Legendre function. We defined the electrical size of the model as kr. Since the Earth's radius is approximately 6370 km, the huge electrical size of the Earth causes the series to converge very slowly [23]. In the small-scale model, the series can converge with a ten-fold magnitude. On the Earth scale, the series is still difficult to converge within the order of tens of millions. To solve the above numerical problem, we took three techniques. The first technique we used was to change the formula form to relieve the memory demand, where the enormous electrical size makes trouble. For the derivative of the spherical Bessel function, we adopt the recursive formula:

$$\begin{aligned} \tfrac{dJ_n(x)}{dx} &= J_{n-1}(x) - \tfrac{n}{x}J_n(x) \\ \tfrac{dH_n(x)}{dx} &= H_{n-1}(x) - \tfrac{n}{x}H_n(x) \end{aligned} \tag{11}$$

To calculate the brackets values in Equation (10) more efficiently, we follow Equation (11) and extract the multiplication of $J_n(x)$ and $H_n(x)$, where the reciprocal connection between them eliminates the considerably large value.

Barrick [23] proposed a fast convergence method that consists of adding and subtracting another series to the solution. The subtracting series is the approximate value of each original series at $n \to \infty$, and the added term is the sum of all approximate values. Based on this idea, we derived the approximate values and the sum of the approximate values of 10 electromagnetic components in the TM and TE wave modes. This problem's specific convergence method was provided, and is abbreviated as the "addition and subtraction" convergence method (see Appendix B).

When using the "addition and subtraction" convergence method, the numerical summation converged when n was greater than 10^6. We introduced the Padé approximant to accelerate the convergence further [35,37]. The series converged when n took a value of 1000 and greatly improved the complexity of our solution.

3. Results

In this section, a comparison between previous results and data measured in the field was performed to verify the accuracy of the formulas and numerical results. We discussed the electromagnetic characteristics of the spherical "Earth-ionosphere" model, compared it with the results of the planar layered model, and analyzed its physical mechanism. In addition, the global electromagnetic radiation map was also given to guide data acquisition in CSELF exploration.

3.1. Correctness Verification

3.1.1. Comparison of the Theoretical Results

The Earth is considered a uniform sphere. Peng [25] gave the numerical results of the electromagnetic field in the spherical waveguide of the Earth-ionosphere. Although the model is not particularly useful for geophysical exploration, it can be used to validate our results. The resistivity of air is 10^{14} Ω·m, the resistivity of the ionosphere is 10^5 Ω·m, and the resistivity of Earth is 1000 Ω·m, corresponding to 0, 1, and −1, respectively, in Figure 2b. The height of the ionosphere from the ground is 85 km, the radius of the Earth is 6370 km, and the electric dipole moment is Idl = 1 A·m, as shown in Figure 2a.

The two results, depicted in Figure 3, were essentially consistent. We further calculated the relative error between our results and those of Peng. The black dotted line shows that the relative error is less than 1%.

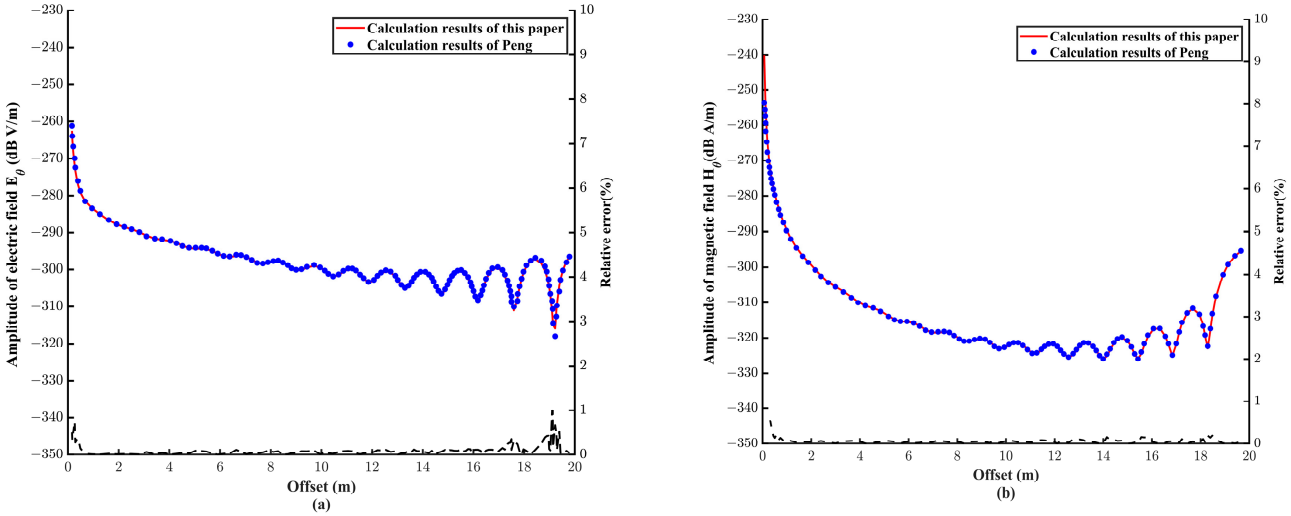

Figure 3. Comparison diagram of the electromagnetic field results. The red curve represents our result. The blue dot represents the results of Peng. The black dotted line is the relative error. (**a**) Tangential electric field E_θ propagation curve. (**b**) Tangential magnetic field H_θ propagation curve.

3.1.2. Comparison of Data Measured in the Field

The measurement conditions specified by Bannister (1973) are as follows [1]: the conductivity of Earth is 2.8×10^{-4} S/m, the angle between the measuring path and source is 15° at a frequency of 45 Hz; the conductivity of Earth is 3.2×10^{-4} S/m, the angle between the measuring path and the source is 19° at a frequency of 75 Hz; and the Wisconsin station is an east–west antenna with a length of 22.5 km and current of 300 A. We simulated the electromagnetic field and then compared the results with the data published for the Wisconsin station.

Figure 4 indicates the agreement between the simulation and the data measured in the field, and only a few points have a slight deviation. The relative error between the theoretical and measured values is less than 2%, as shown on the black dotted line. The model we used is an approximation of the ionosphere, and with the spatial disturbance of the ionosphere and measurement error, we believe that the calculation accuracy of this paper is acceptable.

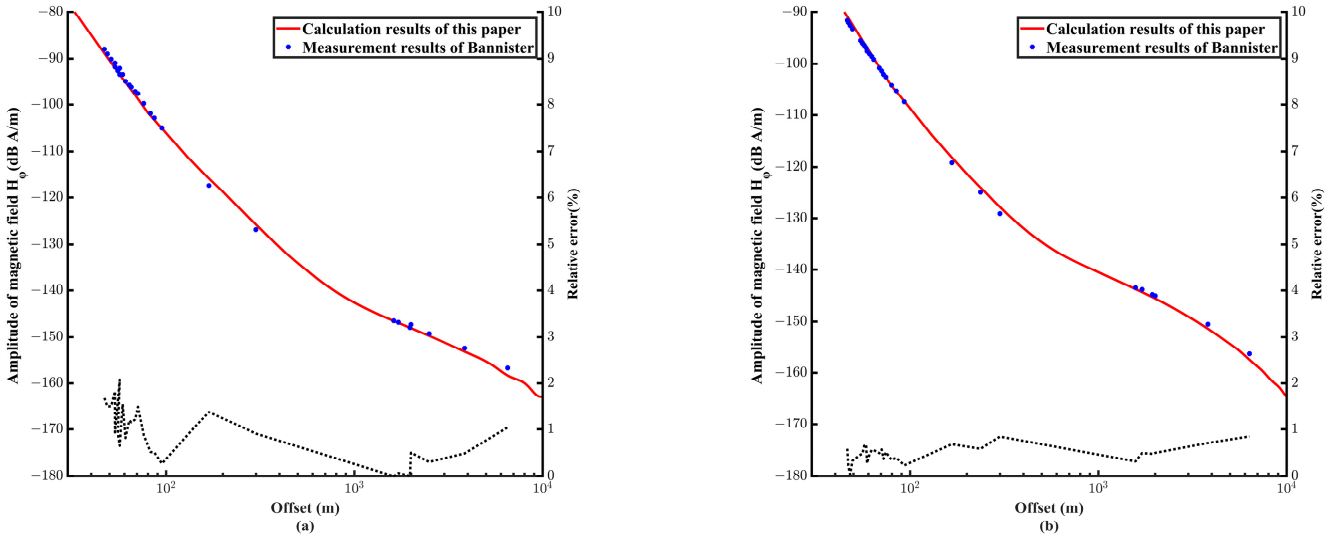

Figure 4. Comparison between the measured in the field and theoretical values. The blue dot represents the data given by Bannister. The red curve represents our calculation result. The black dotted line is the relative error. (**a**) Magnetic field H_φ results at a frequency of 45 Hz. (**b**) Magnetic field H_φ results at a frequency of 75 Hz.

3.2. Analysis of the Electromagnetic Characteristics

3.2.1. Comparison between Planar and Spherical Model

To illustrate the influence of the curvature of the Earth on the electromagnetic field, we compared the calculation results of the planar model [31] and the spherical model based on the resistivity of air and ionosphere. Earth is 10^{14} Ω·m, 10^5 Ω·m, and 1000 Ω·m, the height of the ionosphere from the ground is 100 km, the radius of the Earth is 6370 km, and the electric dipole moment is Idl = 250 A × 50 km. When the source–receiver distance is less than half of the Earth's radius, the influence of the Earth's curvature is small, and the Earth's surface can be approximated to a plane. Figure 5 shows that the calculation results of the two are in good agreement within 3000 km, but the curves diverge with the increase in distance.

It was discovered that the field may oscillate in space with a growing amplitude in the spherical cavity model at greater offset. Contrary to the conventional planar model, the fields on the global scale do not decay with the source–receiver distance. The ionosphere, air, and Earth together make up a horizontal infinite waveguide in a planar layered model; as a result, electromagnetic waves from the source propagate in all directions. In the spherical model, however, the ionosphere, air, and Earth form a closed spherical waveguide.

Electromagnetic waves trapped in the waveguide may produce resonance. In the near-field, resonance is absent because the fields directly emitted from the source are dominant and display only geometrical decay.

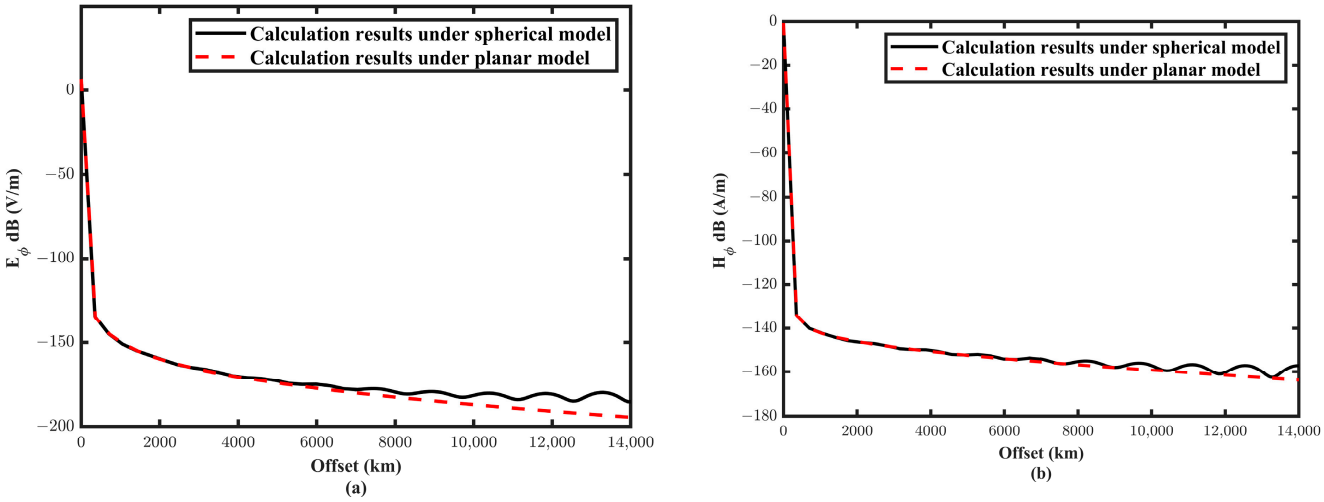

Figure 5. Comparison of electromagnetic fields at a frequency of 100 Hz under the spherical–planar model (**a**,**b**).

3.2.2. Curve Characteristic Analysis

To explain the characteristics of the electromagnetic field under the global spherical "Earth-ionosphere" cavity, we examined the electromagnetic field propagation curves at different frequencies. Under the same model parameters as the previous section, the source was a unit dipole.

Figure 6 illustrates the electromagnetic field propagation rule that the spatial oscillation frequency increases with the temporal frequency. The wavelength is inversely proportional to the frequency. Thus, the higher the frequency, the shorter the wavelength, which results in more antinodes. The fields emitted by the source travel in all directions and arrive in the same phase at the mirror point. As a result, the fields at the mirror point are always the strongest locally.

3.2.3. Radiation Pattern

To further understand the spatial characteristics of the fields emitted by a CSELF source, we investigated the radiation pattern of the fields in 3-D.

Figures 7–10 show the E_ϕ, E_θ, H_θ, and H_ϕ field patterns at 10 Hz. We observed that the fields attenuated slowly in the spherical waveguide region except in the resonant area. A comparison of E_ϕ and E_θ shows that in the Northern Hemisphere, E_θ was less affected by the low value region, whereas in the Southern Hemisphere, E_ϕ was less affected by the low value region. The magnetic field presents similar laws.

Under the influence of the ionosphere, the electromagnetic field emitted by the HED becomes strong in some places and weak in others. Collecting electromagnetic signals in an area with a weakened field strength is bound to be detrimental to studies on underground structures. The electromagnetic waves received on the surface convey both noise and helpful signals carrying underground information. The signal-to-noise ratio will decrease if electromagnetic signals are collected in a region with weak field strength. This further affects the quality of data interpretation. Therefore, drawing electromagnetic field radiation patterns can guide field data acquisition and collect higher-quality signals in strong areas.

3.2.4. The Influence of Ionospheric Structure on Electromagnetic Fields

Although we can equate the ionosphere with a uniform medium with a certain conductivity, its layered structure can also have an impact on the electromagnetic field. The

ionosphere serves as a propagation medium for electromagnetic waves, which are refracted, reflected, dispersed, and absorbed, with some energy lost in the process. Therefore, it is necessary to study the influence of ionospheric structure on electromagnetic fields.

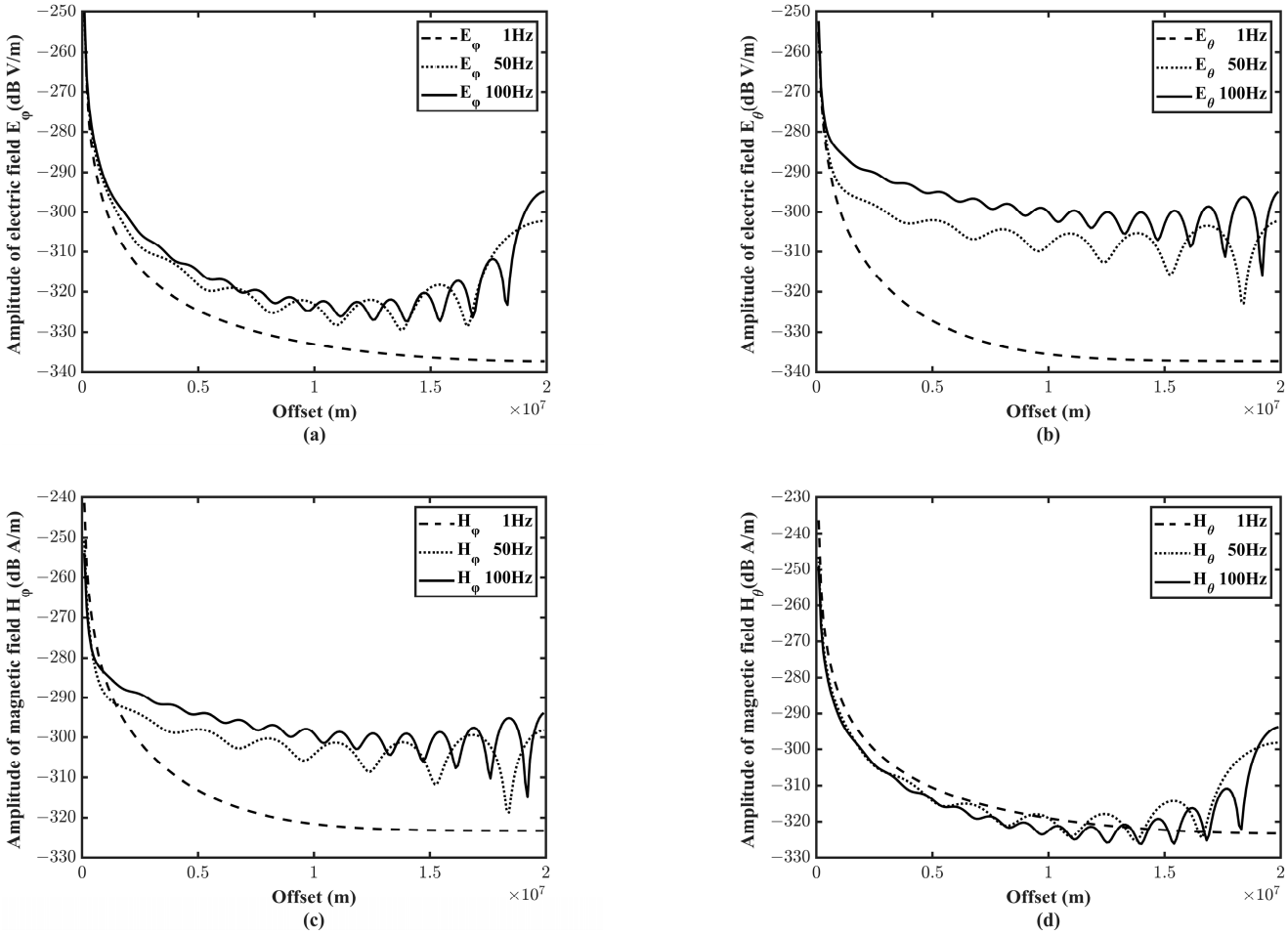

Figure 6. Propagation curve of the electromagnetic field in the waveguide region at 1 Hz, 50 Hz, and 100 Hz,. (**a**) Propagation curve of E_φ. (**b**) Propagation curve of E_θ. (**c**) Propagation curve of H_φ. (**d**) Propagation curve of H_θ.

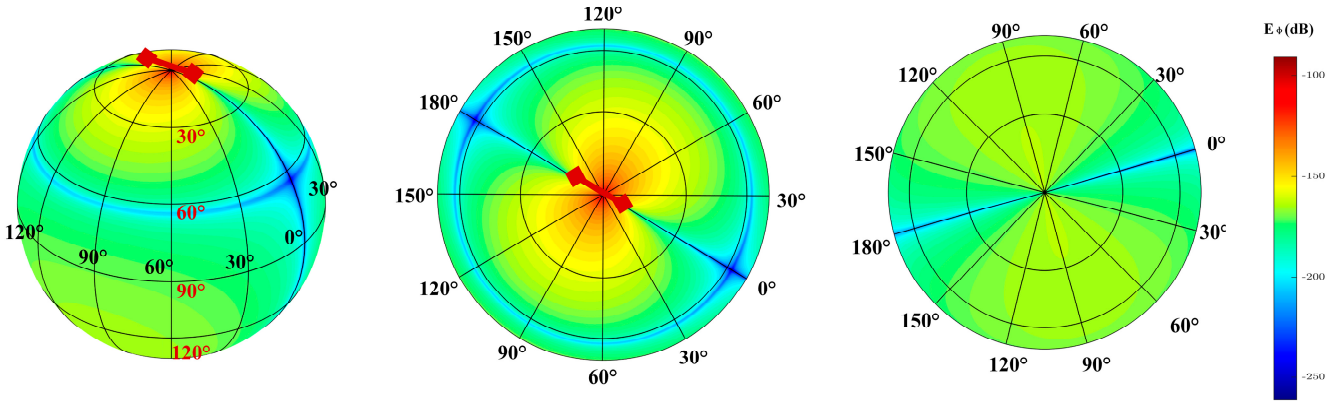

Figure 7. Radiation pattern of E_φ.

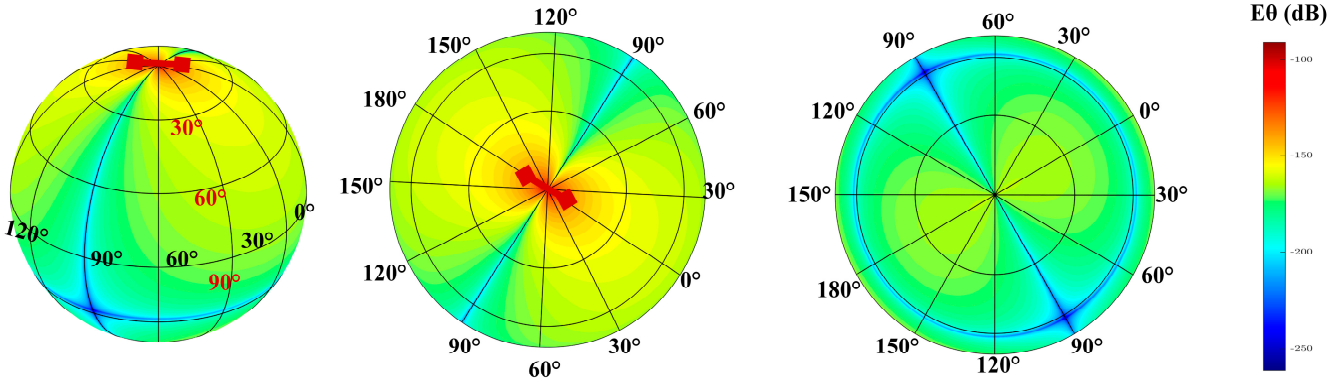

Figure 8. Radiation pattern of E_θ.

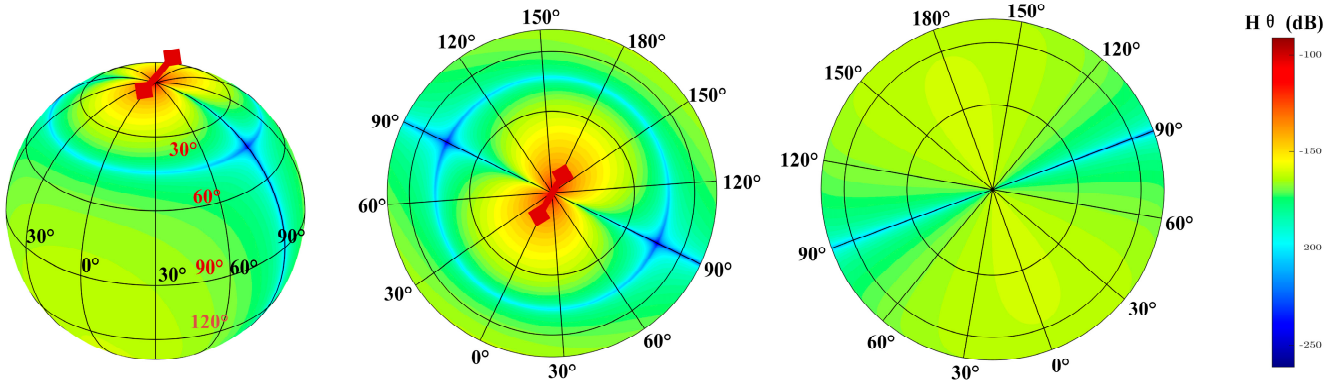

Figure 9. Radiation pattern of H_θ.

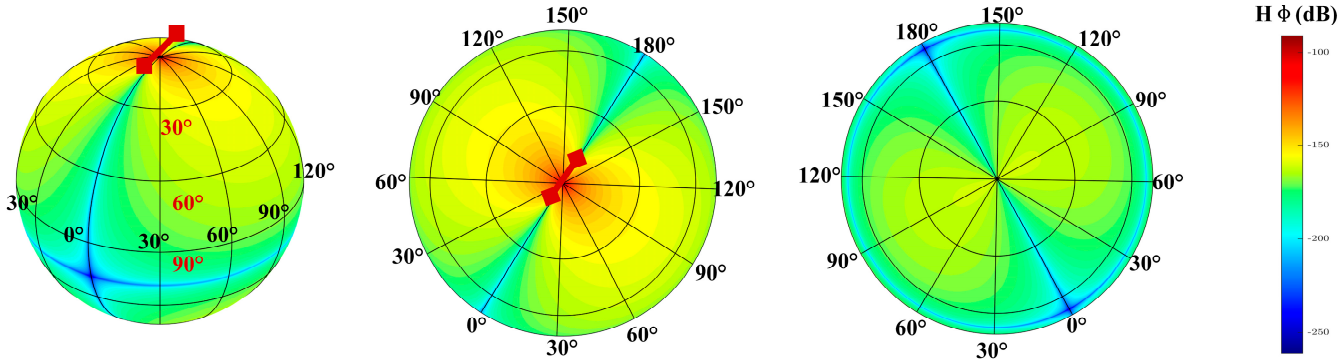

Figure 10. Radiation pattern of H_φ.

We set the conductivity of the ionosphere at 10^{-5} S/m as model U (uniform), which corresponds to σ_1 in Figure 2b. In model G ($\sigma_2 < \sigma_1$), the conductivity of the ionosphere was 10^{-5} S/m and 10^{-7} S/m, corresponding to σ_{-1} and σ_{-2}. In model D ($\sigma_2 > \sigma_1$), the conductivity of the ionosphere was 10^{-5} S/m and 10^{-3} S/m, corresponding to σ_{-1} and σ_{-2}. The conductivity of air was 10^{-14} S/m, and the conductivity of the Earth was 0.001 S/m, corresponding to σ_0 and σ_1 in Figure 2b. The height of the ionosphere from the ground is 85 km, the radius of the Earth is 6370 km, and the electric dipole moment is Idl = 1 A·m, as shown in Figure 2a. We calculated the propagation curves of the electromagnetic field under three different models at a frequency of 100 Hz.

Figure 11 illustrates how various ionospheric structures might alter the electromagnetic field's amplitude. Yet, as the propagation curve's shape is solely determined by frequency, it will have no impact on that. The three curves overlapped at areas with a short offset (about 700 km), as we discovered at the same time. This demonstrates that the ionosphere's impact on the electromagnetic field is negligible under a short offset.

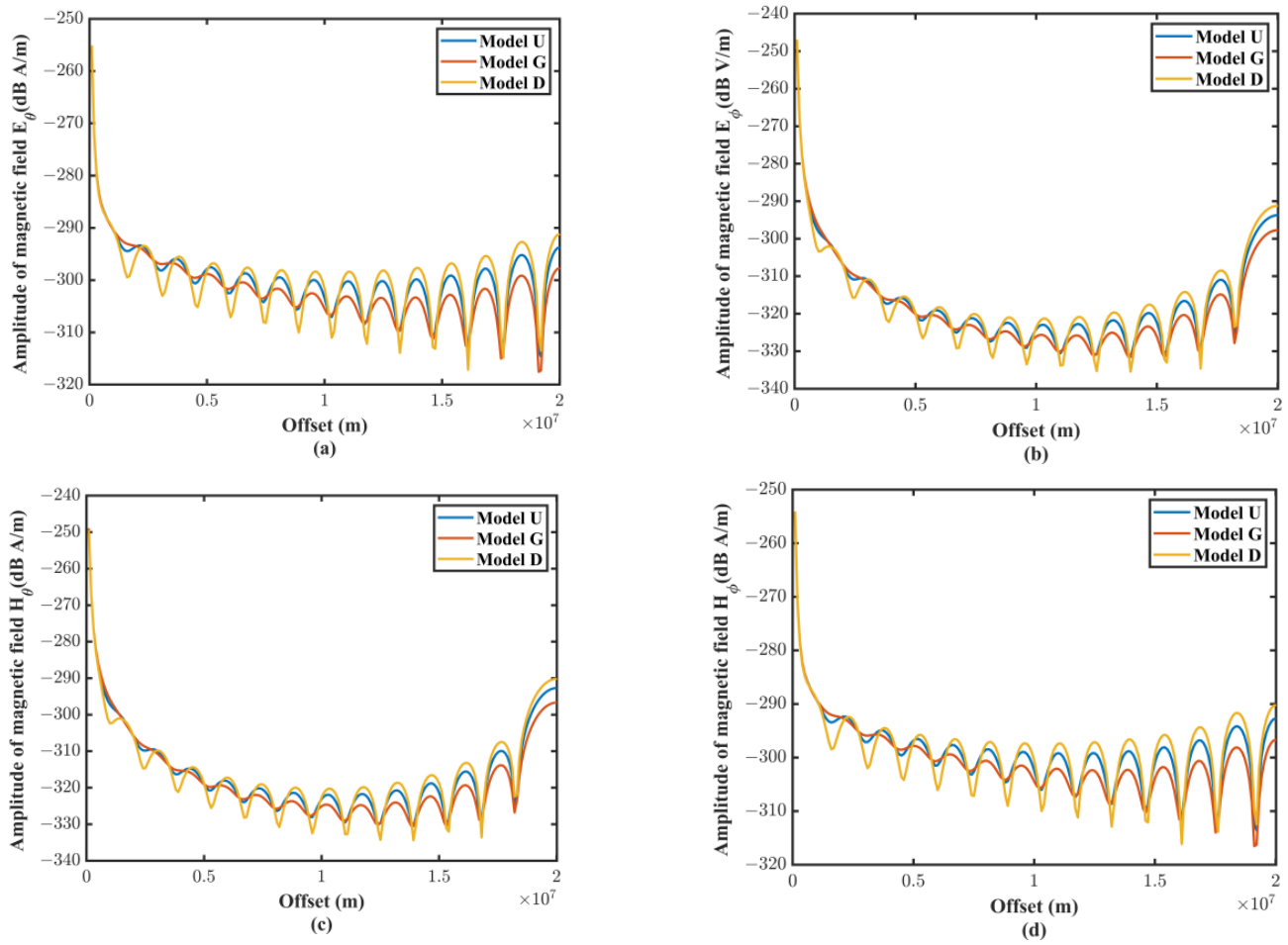

Figure 11. Propagation curve of the electromagnetic field in the waveguide region at 100 Hz: The blue, red, and orange lines represent the electromagnetic fields in the U, G, and D models, respectively. (**a**) Propagation curve of E_θ. (**b**) Propagation curve of E_φ. (**c**) Propagation curve of H_θ. (**d**) Propagation curve of H_φ.

4. Discussion

Following the rules of the MT, by observing the orthogonal electric and magnetic field components, the Cagniard apparent resistivity was computed:

$$\begin{aligned} \rho_{\theta\varphi} &= \frac{1}{\omega\mu}\left|\frac{E_\theta}{H_\varphi}\right|^2 \\ \rho_{\varphi\theta} &= \frac{1}{\omega\mu}\left|\frac{E_\varphi}{H_\theta}\right|^2 \end{aligned} \tag{12}$$

For a given frequency, the partition of the near- and far-field regions depends on the Earth's resistivity value. The lower the Earth's resistivity, the sooner a wave can reach the far-field region. Thus, the Earth resistivity was assigned a value of 10^4 Ω·m to ensure that the predicted far-field region was valid for any practical applications because the real earth resistivity is generally less than 10^4 Ω· m.

Figures 12 and 13 clearly shows that $\rho_{\theta\varphi}$ enters the far-field regions sooner. With a frequency of 0.1 Hz, $\rho_{\varphi\theta}$ converges to the true resistivity value at 2000 km, while $\rho_{\theta\varphi}$ converges at 1500 km. Therefore, we suggest adopting the data acquisition method of apparent resistivity $\rho_{\theta\varphi}$.

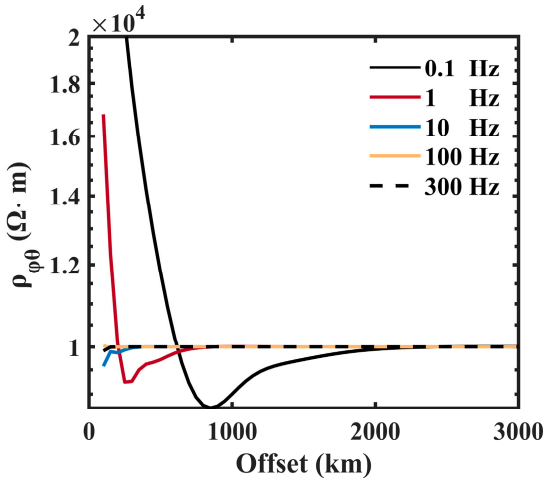

Figure 12. Cagniard apparent resistivity $\rho_{\varphi\theta}$. The black, red, blue, orange, and black dotted lines are the apparent resistivities at 0.1, 1, 10, 100, and 300 Hz, respectively.

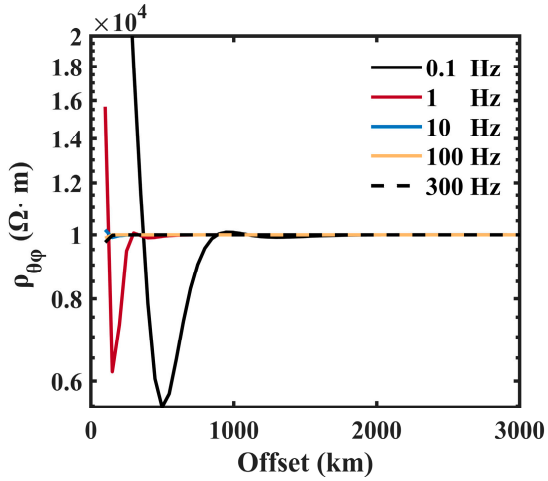

Figure 13. Cagniard's apparent resistivity $\rho_{\theta\varphi}$. The black, red, blue, orange, and black dotted lines are the apparent resistivities at 0.1, 1, 10, 100, and 300 Hz, respectively.

5. Conclusions

The present research aimed to study the electromagnetic field emitted by CSELF and present the exact formulas for a horizontal electric dipole (HED) in a spherical "Earth-ionosphere" space model to expand the coverage of CSELF. We established a new spherical "Earth-ionosphere" full-space model for CSELF. Using the general boundary condition of the electromagnetic field, we obtained an accurate expression in the sum of the series of the spherical Bessel function and the Legendre function through the separation of variables method. This research can also calculate the electromagnetic field under the layered medium.

We assessed three techniques: function combination pairs, addition and subtraction terms, and Padé approximants, to handle slowly converging numerical calculations and achieve a performance boost of 1000 times. The new solution was consistent with the previous numerical results and data measured in the field.

The most prominent finding is that the electromagnetic fields emitted by HED render geometrical attenuation with the source–receiver distance in the near-field regions. However, in the far-field regions, the fields demonstrate resonance, a pattern different from the traditional planar layer model. Finally, we discussed the application conditions of Cagniard's apparent resistivity in CSELF. One of the interesting findings is that the apparent resistivity, $\rho_{\theta\varphi}$, enter the far-field regions sooner than $\rho_{\varphi\theta}$.

A limitation of this study is that we did not consider the actual length and current variation of the transmitting antenna. For the following work, the results in this paper can be used as Green's functions to simulate the electromagnetic field of actual antennas and 3-D models.

Author Contributions: Conceptualization, Q.-Y.D. and Y.G.; methodology, Y.G.; validation, Y.G. and C.-M.F.; writing—original draft preparation, Y.G.; writing—review and editing, Y.-L.Z.; All authors have read and agreed to the published version of the manuscript.

Funding: This research was funded by the National Key R&D Program of China (Grant No. 2022YFF0706200), the Strategic Priority Research Program of the Chinese Academy of Sciences (XDA14050300), and the National Natural Science Foundation of China (NSFC: # 41874088).

Data Availability Statement: If you are interested in the results in the article and wish to obtain simulation data, you can contact the first author: gaoya@mail.iggcas.ac.cn (Y.G.).

Acknowledgments: The authors thank the anonymous reviewers and editors for their valuable suggestions.

Conflicts of Interest: The authors declare no conflict of interest.

Appendix A

The expression of the coefficients:

$$\begin{aligned} R_{i,i+1}^{TM} &= \frac{k_i\widetilde{\varepsilon}_{i+1}H_n^{(1)}(k_{i+1}a)H_n'(k_ia)-k_{i+1}\widetilde{\varepsilon}_iH_n'(k_{i+1}a)H_n^{(1)}(k_ia)}{k_{i+1}\widetilde{\varepsilon}_iJ_n(k_ia)H_n'(k_{i+1}a)-k_i\widetilde{\varepsilon}_{i+1}J_n'(k_ia)H_n^{(1)}(k_{i+1}a)} \\ T_{i,i+1}^{TM} &= \frac{ik_{i+1}\widetilde{\varepsilon}_{i+1}}{k_{i+1}\widetilde{\varepsilon}_iJ_n(k_ia)H_n'(k_{i+1}a)-k_i\widetilde{\varepsilon}_{i+1}J_n'(k_ia)H_n^{(1)}(k_{i+1}a)} \\ R_{i,i+1}^{TE} &= \frac{k_i\mu_{i+1}H_n^{(1)}(k_{i+1}a)H_n'(k_ia)-k_{i+1}\mu_iH_n^{(1)}(k_ia)H_n'(k_{i+1}a)}{k_{i+1}\mu_iH_n'(k_{i+1}a)J_n(k_ia)-k_i\mu_{i+1}H_n^{(1)}(k_{i+1}a)J_n'(k_ia)} \\ T_{i,i+1}^{TE} &= \frac{ik_{i+1}\mu_{i+1}}{k_{i+1}\mu_iH_n'(k_{i+1}a)J_n(k_ia)-k_i\mu_{i+1}H_n^{(1)}(k_{i+1}a)J_n'(k_ia)} \end{aligned} \tag{A1}$$

$$\begin{aligned} T_{i,i-1}^{TM} &= \frac{ik_{i-1}\widetilde{\varepsilon}_{i-1}}{k_i\widetilde{\varepsilon}_{i-1}J_n(k_{i-1}a)H_n'(k_ia)-k_{i-1}\widetilde{\varepsilon}_iJ_n'(k_{i-1}a)H_n^{(1)}(k_ia)} \\ R_{i,i-1}^{TM} &= \frac{k_{i-1}\widetilde{\varepsilon}_iJ_n'(k_{i-1}a)J_n(k_ia)-k_i\widetilde{\varepsilon}_{i-1}J_n'(k_ia)J_n(k_{i-1}a)}{k_i\widetilde{\varepsilon}_{i-1}J_n(k_{i-1}a)H_n'(k_ia)-k_{i-1}\widetilde{\varepsilon}_iJ_n'(k_{i-1}a)H_n^{(1)}(k_ia)} \\ T_{i,i-1}^{TE} &= \frac{ik_{i-1}\mu_{i-1}}{k_i\mu_{i-1}J_n(k_{i-1}a)H_n'(k_ia)-k_{i-1}\mu_iJ_n'(k_{i-1}a)H_n^{(1)}(k_ia)} \\ R_{i,i-1}^{TE} &= \frac{k_{i-1}\mu_iJ_n(k_ia)J_n'(k_{i-1}a)-k_i\mu_{i-1}J_n(k_{i-1}a)J_n'(k_ia)}{k_i\mu_{i-1}J_n(k_{i-1}a)H_n'(k_ia)-k_{i-1}\mu_iJ_n'(k_{i-1}a)H_n^{(1)}(k_ia)} \end{aligned} \tag{A2}$$

where we take $\widetilde{\varepsilon} = \sigma - i\omega\varepsilon$ and a is height of interface.

$$\widetilde{R}_{i,i+1} = R_{i,i+1} + \frac{T_{i+1,i}\widetilde{R}_{i+1,i+2}T_{i,i+1}}{1 - R_{i+1,i}\widetilde{R}_{i+1,i+2}} \tag{A3}$$

$$\widetilde{R}_{i,i-1} = R_{i,i-1} + \frac{T_{i-1,i}\widetilde{R}_{i-1,i-2}T_{i,i-1}}{1 - R_{i-1,i}\widetilde{R}_{i-1,i-2}} \tag{A4}$$

$$M_i = \frac{1}{1 - R_{i,i-1}R_{i,i+1}} \tag{A5}$$

$$T_{1,N} = S_{1,2}S_{2,3}\cdots S_{N-2,N-1}T_{N-1,N} \tag{A6}$$

$$S_{i,i+1} = \frac{T_{i,i+1}}{1 - R_{i+1,i}\widetilde{R}_{i+1,i+2}} \tag{A7}$$

Appendix B

Approximate value of each electromagnetic component and their sum.

For TE polarized waves:

(1) E_r

$$E_r(n) = (2n+1)\left(\frac{r}{b}\right)^{n+1}\frac{ik_2k_1^2}{k_2^2+k_1^2}P_n^1(\cos\theta) \tag{A8}$$

$$\begin{aligned} SE_r &= \sum_{n=1}^{\infty}(2n+1)\left(\tfrac{r}{b}\right)^{n+1}\tfrac{ik_2k_1^2}{k_2^2+k_1^2}P_n^1(\cos\theta) \\ &= \tfrac{r}{b}\tfrac{ik_2k_1^2}{k_2^2+k_1^2}\left(\tfrac{3yt}{g^3}+\tfrac{6yt^2(x-t)}{g^5}\right) \end{aligned} \tag{A9}$$

(2) E_φ^{TM}

$$E_\varphi^{TM}(n) = \frac{(2n+1)}{n}\frac{1}{b}\left(\frac{r}{b}\right)^{n}\frac{ik_2k_1^2}{k_2^2+k_1^2}P_n^1(\cos\theta) \tag{A10}$$

$$\begin{aligned} SE_\varphi^{TM} &= \sum_{n=1}^{\infty}\tfrac{(2n+1)}{n}\tfrac{1}{b}\left(\tfrac{r}{b}\right)^{n}\tfrac{ik_2k_1^2}{k_2^2+k_1^2}P_n^1(\cos\theta) \\ &= \tfrac{1}{b}\tfrac{ik_2k_1^2}{k_2^2+k_1^2}\left(\tfrac{x}{y}+\tfrac{t-x}{yg}+2\tfrac{yt}{g^3}\right) \end{aligned} \tag{A11}$$

(3) H_φ^{TM}

$$H_\varphi^{TM}(n) = \frac{(2n+1)}{n(\mathrm{n}+1)}\left(\frac{r}{b}\right)^{n+1}\frac{ik_2k_1^2}{k_2^2+k_1^2}\frac{\partial}{\partial\theta}P_n^1(\cos\theta) \tag{A12}$$

$$\begin{aligned} SH_\varphi^{TM} &= \tfrac{r}{b}\tfrac{ik_2k_1^2}{k_2^2+k_1^2}\sum_{n=1}^{\infty}\tfrac{(2n+1)}{n(\mathrm{n}+1)}\left(\tfrac{r}{b}\right)^{n}\tfrac{\partial}{\partial\theta}P_n^1(\cos\theta) \\ &= \tfrac{r}{b}\tfrac{ik_2k_1^2}{k_2^2+k_1^2}\left(\tfrac{1-t^2}{g^3}-1\right)-\tfrac{r}{b}\tfrac{ik_2k_1^2}{k_2^2+k_1^2}\tfrac{\cos\theta}{\sin\theta}\left(\tfrac{xt+1}{yt}+\tfrac{t^2-1}{ytg}\right) \end{aligned} \tag{A13}$$

(4) H_θ^{TM}

$$H_\theta^{TM}(n) = \frac{(2n+1)}{n(\mathrm{n}+1)}\left(\frac{r}{b}\right)^{n+1}\frac{ik_2k_1^2}{k_2^2+k_1^2}P_n^1(\cos\theta) \tag{A14}$$

$$\begin{aligned} SH_\theta^{TM} &= \sum_{n=1}^{\infty}\tfrac{(2n+1)}{n(\mathrm{n}+1)}\left(\tfrac{r}{b}\right)^{n+1}\tfrac{ik_2k_1^2}{k_2^2+k_1^2}P_n^1(\cos\theta) \\ &= \tfrac{r}{b}\tfrac{ik_2k_1^2}{k_2^2+k_1^2}\left(\tfrac{xt+1}{yt}+\tfrac{t^2-1}{ytg}\right) \end{aligned} \tag{A15}$$

(5) E_θ^{TM}

$$E_\theta^{TM}(n) = \frac{1}{b}\frac{(2n+1)}{n}\left(\frac{r}{b}\right)^{n}\frac{ik_2k_1^2}{k_2^2+k_1^2}\frac{d}{d\theta}P_n^1(\cos\theta) \tag{A16}$$

$$\begin{aligned} SE_\theta^{TM} = \tfrac{1}{b}\tfrac{ik_2k_1^2}{k_2^2+k_1^2}[&2\tfrac{t_b(x+x^2t_b-xt_b^2-2t_b+t_b^3)}{g_b^5} \\ &+3\tfrac{t_b(x-t_b)}{g_b^3}+\tfrac{1}{g_b}-1-\tfrac{\cos\theta}{\sin\theta}\left(2\tfrac{yt_b}{g_b^3}+\tfrac{x}{y}+\tfrac{t_b-x}{yg_b}\right)] \end{aligned} \tag{A17}$$

For TE polarized waves:

(1) H_r

$$H_r(n) = -ik_2r\left(\frac{r}{b}\right)^{n}P_n^1(\cos\theta) \tag{A18}$$

$$\begin{aligned} SH_r &= -ik_2r\sum_{n=1}^{\infty}\left(\tfrac{r}{b}\right)^{n}P_n^1(\cos\theta) \\ &= -ik_2r\tfrac{yt}{g^3} \end{aligned} \tag{A19}$$

(2) E_φ^{TE}

$$E_\varphi^{TE}(n) = \frac{-ik_2r}{n(\mathrm{n}+1)}\left(\frac{r}{b}\right)^{n}\frac{\partial}{\partial\theta}P_n^1(\cos\theta) \tag{A20}$$

$$\begin{aligned} SE_{\varphi}^{TE} &= -ik_2 r \sum_{n=1}^{\infty} \frac{1}{n(n+1)} \left(\frac{r}{b}\right)^n \frac{\partial}{\partial\theta} P_n^1(\cos\theta) \\ &= -ik_2 r[(\frac{1}{g_b} - 1) - \frac{\cos\theta}{\sin\theta}(\frac{x}{y} + \frac{g_b - 1}{y t_b})] \end{aligned} \tag{A21}$$

(3) H_{θ}^{TE}

$$H_{\theta}^{TE}(n) = -ik_2 \frac{1}{n} \left(\frac{r}{b}\right)^n \frac{\partial}{\partial\theta} P_n^1(\cos\theta) \tag{A22}$$

$$\begin{aligned} SH_{\theta}^{TE} &= -ik_2 \sum_{n=1}^{\infty} \frac{1}{n} \left(\frac{r}{b}\right)^n \frac{\partial}{\partial\theta} P_n^1(\cos\theta) \\ &= -ik_2[(\frac{1 - x t_b}{g_b^3} - 1) - \frac{\cos\theta}{\sin\theta}(\frac{x}{y} + \frac{t_b - x}{y g_b})] \end{aligned} \tag{A23}$$

(4) H_{φ}^{TE}

$$H_{\varphi}^{TE}(n) = \frac{-ik_2}{n} \left(\frac{r}{b}\right)^n P_n^1(\cos\theta) \tag{A24}$$

$$\begin{aligned} SH_{\varphi}^{TE} &= -ik_2 \sum_{n=1}^{\infty} \frac{1}{n} \left(\frac{r}{b}\right)^n P_n^1(\cos\theta) \\ &= -ik_2(\frac{x}{y} + \frac{t_b - x}{y g_b}) \end{aligned} \tag{A25}$$

(5) E_{θ}^{TE}

$$E_{\theta}^{TE}(n) = \frac{-ik_2 r}{n(n+1)} \left(\frac{r}{b}\right)^n P_n^1(\cos\theta) \tag{A26}$$

$$\begin{aligned} SE_{\theta}^{TE} &= \sum_{n=1}^{\infty} \frac{-ik_2 r}{n(n+1)} (t_b)^n P_n^1(\cos\theta) \\ &= -ik_2 r(\frac{x}{y} + \frac{g_b - 1}{y t_b}) \end{aligned} \tag{A27}$$

Among $x = \cos\theta$, $t_b = \frac{r}{b}$, $g_b = \sqrt{1 - 2xt + t^2}$ and $y = \sqrt{1 - x^2}$.

Note: The symbol *A(n)* represents the approximate value, and *SA* represents the series sum of infinite term approximate value. Lower subscript 1 represents the underground medium parameters, and lower subscript 2 represents the air layer parameters.

References

1. Wait, J.R. On the theory of mixed-path ground-wave propagation on a spherical earth. *J. Res. Natl. Bur. Stand. Sect. D Radio Propag.* **1961**, *65*, 401. [CrossRef]
2. Wait, J.R. Transmission and reflection of electromagnetic waves in the presence of stratified media. *J. Res. Natl. Bur. Stand.* **1958**, *61*, 205–232. [CrossRef]
3. Galejs, J. *Terrestrial Propagation of Long Electromagnetic Waves*; Pergamon Press: Oxford, UK, 1972.
4. Galejs, J. Horizontally oriented antennas in the presence of an anisotropic ground. *Radio Sci.* **1969**, *4*, 1047–1059. [CrossRef]
5. Wagner, L.S.; Goldstein, J.A.; Rupar, M.A.; Kennedy, E.J. Delay, Doppler, and amplitude characteristics of HF signals received over a 1300-km transauroral sky wave channel. *Radio Sci.* **2016**, *30*, 659–676. [CrossRef]
6. Burrows, M.; Niessen, C. ELF communication system design. In Proceedings of the Ocean 72—IEEE International Conference on Engineering in the Ocean Environment, Newport, RI, USA, 13–15 September 1972; pp. 95–109. [CrossRef]
7. Lu, J.X. *Very Low Frequency and Ultra Low Frequency Radio Technology*; Harbin Engineering University Press: Harbin, China, 2012.
8. Barr, R.; Jones, D.L.; Rodger, C.J. ELF and VLF radio waves. *J. Atmos. Sol.-Terr. Phys.* **2000**, *62*, 1689–1718. [CrossRef]
9. Witvliet, B.A.; Alsina-Pages, R.M. Radio communication via Near Vertical Incidence sky-wave propagation: An overview. *Elecommun. Syst.* **2017**, *66*, 295–309. [CrossRef]
10. Bannister, P.R.; Wolkoff, E.A.; Katan, J.R.; Williams, F.J. Far-field, extremely-low-frequency propagation measurements. *Radio Sci.* **1973**, *8*, 623–631. [CrossRef]
11. Bannister, P.R.; Katan, J.R.; Wolkoff, E.A.; Kraimer, W.A. Farfield extremely low frequency propagation measurements, May 1972. In *Farfield Extremely Low Frequency Propagation Measurements*; Naval Underwater Systems Center New London Conn New London Lab: London, UK, 1974.
12. Bannister, P. ELF propagation update. *IEEE J. Ocean. Eng.* **1984**, *9*, 179–188. [CrossRef]
13. Bernstein, S.L.; Burrows, M.L.; Evans, J.E.; Griffiths, A.S.; McNeill, D.A.; Niessen, C.W.; Richer, I.; White, D.P.; Willim, D.K. Long-range communications at extremely low frequencies. *Proc. IEEE* **1974**, *62*, 292–312. [CrossRef]

14. Bernstein, S.; McNeill, D.; Richer, I. A signaling scheme and experimental receiver for extremely low frequency (ELF) communication. *IEEE Trans. Commun.* **1974**, *22*, 508–528. [CrossRef]
15. Galejs, J. A further note on terrestrial extremely low-frequency propagation in the presence of an isotropic ionosphere with an exponential conductivity-height profile. *J. Geophys. Res.* **1962**, *67*, 2715–2728. [CrossRef]
16. Rowe, H.E. Extremely low frequency (ELF) communication to submarines. *IEEE Trans. Commun.* **1974**, *22*, 371–385. [CrossRef]
17. Goldstein, M.A.; Strangway, D.W. Audio-frequency magnetotellurics with a grounded electric dipole source. *Geophysics* **1975**, *40*, 669–683. [CrossRef]
18. Field, E.C. Propagation of ELF waves under normal and naturally disturbed conditions. *J. Geophys. Res.* **1969**, *74*, 3639–3650. [CrossRef]
19. Shellman, C.H. A model for propagation of ELF waves throughout the lateral extent of the inhomogeneous Earth-ionosphere wave guide. *Radio Sci.* **1989**, *24*, 35–46. [CrossRef]
20. Fock, V. *Diffraction of Radio Waves Around the Earth's Surface*; Defence Research Information Centre Orpington: Salisbury, UK, 1945; Volume 15, pp. 479–496.
21. Mushtak, V.C.; Williams, E.R. ELF propagation parameters for uniform models of the Earth–ionosphere wave guide. *J. Atmos. Sol.-Terr. Phys.* **2002**, *64*, 1989–2001. [CrossRef]
22. Cummer, S.A. Modeling electromagnetic propagation in the earth-ionosphere wave guide. *IEEE Trans. Antennas Propag.* **2000**, *48*, 1420–1429. [CrossRef]
23. Barrick, D.E. Exact ULF/ELF dipole field strengths in the Earth-ionosphere cavity over the Schumann resonance region: Idealized boundaries. *Radio Sci.* **1999**, *34*, 209–227. [CrossRef]
24. Tao, W.; Pan, W.Y.; Guo, L.X. Numerical integral method for ELF fields excited by vertical electric dipole in asymmetric earth-ionosphere cavity. *Dianbo Kexue Xuebao Chin. J. Radio Sci.* **2012**, *22*, 333–338.
25. Peng, H.Y.; Pan, W.Y.; Guo, L.X. Legendre function series method for ELF fields excited by horizontal electric dipole in earth-ionosphere cavity. *Chin. J. Radio Sci.* **2013**, *28*, 853–858. [CrossRef]
26. Pan, W.; Li, K. *Propagation of SLF/ELF Electromagnetic Waves*; Zhejiang University Press: Hangzhou, China, 2013.
27. Pilipenko, V.A.; Parrot, M.; Fedorov, E.N.; Mazur, N.G. Electromagnetic field in the upper ionosphere from ELF ground-based transmitter. *J. Geophys. Res. A. Space Phys. JGR* **2019**, *124*, 8066–8080. [CrossRef]
28. Di, Q.; Zhu, R.; Xue, G.; Yin, C.; Li, X. New development of the Electromagnetic (EM) methods for deep exploration. *Chin. J. Geophys.* **2019**, *62*, 2128–2138. [CrossRef]
29. Di, Q.; Xue, G.; Yin, C.; Li, X. New methods of controlled-source electromagnetic detection in China. *Sci. China Earth Sci.* **2020**, *63*, 1268–1277. [CrossRef]
30. Di, Q.; Fu, C.; Xue, G.; Wang, M.; An, Z.; Wang, R.; Wang, Z.; Lei, D.; Zhuo, X. Insight into sky-wave theory and breakthrough applications in resource exploration. *Natl. Sci. Rev.* **2021**, *8*, nwab046. [CrossRef]
31. Li, D.; Di, Q.; Wang, M.; Nobes, D. 'Earth–ionosphere' mode controlled source electromagnetic method. *Geophys. J. Int.* **2015**, *202*, 1848–1858. [CrossRef]
32. Velikhov, E.P.; Zhamaletdinov, A.A.; Shevtsov, A.N.; Tokarev, A.D.; Kononov, Y.M.; Pesin, L.B.; Kadyshevich, G.M.; Pertel, M.I.; Veshchev, A.V. Deep electromagnetic studies with the use of powerful ELF radio installations. *Izv. Phys. Solid Earth C/C Fiz. Zemli-Ross. Akad. Nauk.* **1998**, *34*, 615–632.
33. Fu, C.M.; Di, Q.Y.; Wang, M.Y. Calculate electromagnetic fields in stratified medium with layer-matrix method. *Chin. J. Geophys.* **2010**, *53*, 177–188.
34. Srivastava, S.P. Theory of the magnetotelluric method for a spherical conductor. *Geophys. J. Int.* **1966**, *11*, 373–387. [CrossRef]
35. Gao, Y.; Di, Q.; Wang, R.; Fu, C.; Liang, P.; Zheng, F. Strength of the electric dipole source field in multilayer spherical media. *IEEE Trans. Geosci. Remote Sens.* **2021**, *60*, 5902612. [CrossRef]
36. Zheng, F.; Di, Q.; Fu, C. A Spherical "Earth–Ionosphere" Model for Deep Resource Exploration Using Artificial ELF-EM Field. *Remote Sens.* **2022**, *14*, 3088. [CrossRef]
37. Baker, G.A.; Baker, G.A., Jr.; Baker, G.; Graves-Morris, P.; Baker, S.S. *Pade Approximants: Encyclopedia of Mathematics and It's Applications*; Cambridge University Press: Cambridge, UK, 1996; Volume 59.
38. Ginsberg, L. Extremely low frequency (ELF) propagation measurements along a 4900-km path. *IEEE Trans. Commun.* **1974**, *22*, 452–457. [CrossRef]
39. Chew, W.C. *Waves and Fields in Inhomogeneous Media*; IEEE Press: New York, NY, USA, 1995.

Disclaimer/Publisher's Note: The statements, opinions and data contained in all publications are solely those of the individual author(s) and contributor(s) and not of MDPI and/or the editor(s). MDPI and/or the editor(s) disclaim responsibility for any injury to people or property resulting from any ideas, methods, instructions or products referred to in the content.